Synthetic jet actuation for load control

H de Vries, E T A van der Weide and H W M Hoeijmakers

Group Engineering Fluid Dynamics, J. M. Burgers Center for Fluid Dynamics, University of Twente, Enschede, The Netherlands

E-mail: h.devries-1@utwente.nl

Abstract. The reduction of wind turbine blade loads is an important issue in the reduction of the costs of energy production. Reduction of the loads of a non-cyclic nature requires so-called smart rotor control, which involves the application of distributed actuators and sensors to provide fast and local changes in aerodynamic performance. This paper investigates the use of synthetic jets for smart rotor control. Synthetic jets are formed by ingesting low-momentum fluid from the boundary layer along the blade into a cavity and subsequently ejecting this fluid with a higher momentum. We focus on the observed flow phenomena and the ability to use these to obtain the desired changes of the aerodynamic properties of a blade section. To this end, numerical simulations and wind tunnel experiments of synthetic jet actuation on a non-rotating NACA0018 airfoil have been performed. The synthetic jets are long spanwise slits, located close to the trailing edge and directed perpendicularly to the surface of the airfoil. Due to limitations of the present experimental setup in terms of performance of the synthetic jets, the main focus is on the numerical flow simulations. The present results show that high-frequency synthetic jet actuation close to the trailing edge can induce changes in the effective angle of attack up to approximately 2.9°.

1. Introduction

A major goal for the wind energy industry is reduction of the costs of energy production. Important factors affecting these costs are the amount of materials required for the structure, the required maintenance and the reliability of the wind turbine during its life span. One of the contributions to these factors is the design of the wind turbine blades, which is strongly influenced by the fatigue loads they endure. The blades are constantly subjected to changing loads due to variable wind (gusts), turbulent inflow, wind shear, gravity, tower shadow, yaw and wake interaction. In order to reduce the costs of energy production, it is essential to reduce (the amplitude of) these loads [1].

Individual Pitch Control, whereby the pitch angle of each individual blade can be adjusted, enables the reduction of blade loads, mainly those of a periodic nature. However, reduction of the loads of a non-cyclic nature (turbulence, wind gusts) requires so-called smart rotor control. Smart rotor control involves the application of distributed actuators and sensors coupled to one or more controllers, providing fast and local changes in aerodynamic performance of the blades.

Simulations for a 5 MW reference turbine show that smart rotor control, using three trailing edge flaps per blade covering 18% of the blade span, can reduce the fatigue damage equivalent load by 14% to 27%. For the same conditions, Individual Pitch Control only gives a reduction of 2-5% [2]. Other examples of smart rotor control that are presently investigated are for example: (continuous) camber control, micro tabs (small distributed deployable Gurney flaps), plasma actuators and synthetic jets. See Johnson et al.[3, 4], and references cited therein, for an extensive overview of active load control techniques.

The present paper deals with the possible application of synthetic jets for load control. A synthetic jet consists of a cavity below the surface of the blade, with a hole or slit that connects the cavity with the outside world, see figure 1. Due to the periodic motion of one of the cavity walls, low momentum fluid from the boundary layer along the blade is ingested into the cavity and subsequently ejected with a higher momentum [5]. Unlike continuous fluidic jets or pulsed jets, which could also be used for load control [6], synthetic jets do not need an external source of working fluid. Additional systems and complex piping are therefore avoided.

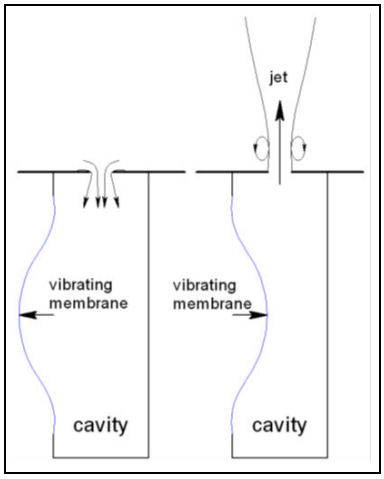

Figure 1. Sketch of a synthetic jet during ingestion (left) and ejection (right).

We focus on the observed flow phenomena and the ability to use these to obtain the desired changes of the aerodynamic properties of a blade section. To this end, numerical simulations and wind tunnel experiments of synthetic jet actuation on a non-rotating NACA0018 airfoil have been performed. The results of a numerical parameter study will be the main topic of this paper. Due to limitations of the experimental setup, we will only briefly address the results of the experiments.

2. Physics of Synthetic Jet Actuation

2.1. Separation vs. Load Control

In the field of external aerodynamics, synthetic jet actuation has been investigated mainly as a means to prevent or delay the onset of boundary layer separation, see for example [7] for a numerical study of synthetic jet actuation close to the leading edge of an airfoil. In a recent experimental study by Maldonado et al. [8], synthetic jet actuation was applied on the suction side of a wind turbine blade at a chordwise location of $x/c = 0.25$, i.e. also close to the leading edge. The jets originated from rectangular orifices, which were oriented such that they were aligned in pairs at an angle of 20° to the flow. Such a configuration leads to the formation of counter-rotating streamwise vortices. These vortices cause transfer of high momentum fluid towards the wall. The effect of synthetic jet actuation in these cases is an increase of the stall angle of attack. For smaller angles of attack, the effects are minimal.

For load control, it is required to change the aerodynamic characteristics over a wide range of angles of attack. In this area of research, synthetic jets have mainly been used to control a region with vorticity near the trailing edge, which has been created by other means, such as a wedge shaped obstacle [10–12] or a Gurney flap [13]. An other example is described by Lopez et al. [9], who performed numerical simulations for a NACA4415 airfoil with a modified trailing edge in which synthetic jets actuators are integrated, see figure 2. These jets are directed tangentially to the upper and lower surface and manipulate the vortical flow regions formed close to the trailing edge. This modifies the flow close to the trailing edge such that the direction in which the flow leaves the trailing edge is manipulated. This directly affects the circulation of the airfoil and thereby the pressure distribution, leading

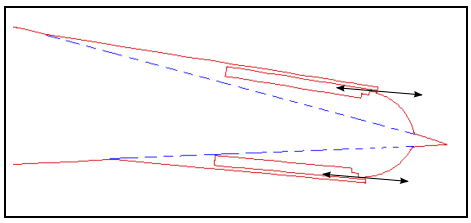

Figure 2. Modified NACA4415 airfoil with integrated synthetic jet actuators [9].

to changes in the aerodynamic properties of the airfoil.

2.2. Actuation Time Scale
The characteristic time scale of the actuation is important for its effectiveness [14, 15]. For separation control, the actuation time scale can be of the order of the convective time scale, $T_{conv} = c/U_\infty$, which couples to the instability of the separating shear layer and the wake. This results in a deflection of the separating shear layer towards the surface of the airfoil and is associated with an increase in the time-average lift. The corresponding dimensionless actuation frequency, $f_j c/U_\infty$, which is referred to as F^+, is in the order of 1. The time scale of actuation can also be one order of magnitude smaller than the convective time scale, i.e. $F^+ = \mathcal{O}(10)$. This is associated with "trapped vorticity" that can locally increase the apparent camber of the airfoil such that a favorable pressure gradient is obtained, which can delay or prevent flow separation. Depending on the location of the synthetic jets, this mechanism can be used for separation control as well as load control.

3. Approach

In the present study, we investigate the possibility of load control by synthetic jet actuation in a different manner than described in section 2.1. Here, the synthetic jets are also located near the trailing edge of the airfoil, but directed perpendicularly to the surface instead of tangentially. The trailing edge has not been modified and no additional obstacles have been added to it. The aim is to let the synthetic jets force flow separation in a time periodic manner, thereby changing the flow near the trailing edge such that the time-averaged circulation of the airfoil is increased or decreased, depending on the side on which the synthetic jets are located. In the present paper the case of two-dimensional flow is investigated, i.e. the synthetic jets are long slits with width w_j, located at a certain chord-wise location x_j/c, see figure 3. For load control, increases in lift as well as decreases in lift are needed. Although both effects could be generated by synthetic jet actuation, we focus on lift increases here, i.e. positive angles of attack are investigated with synthetic jets located on the lower side of the NACA0018 airfoil.

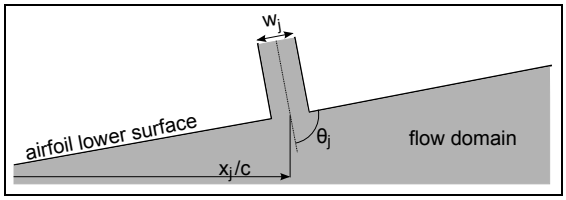

Figure 3. Geometric parameters for long slits.

3.1. Dimensionless Parameters
Assuming the effect of a synthetic jet can be characterized by its output at the exit of the slit, we define an average ejection velocity $\bar{U}_j$ and an average ejection density $\bar{\rho}_j$, as follows

$$\bar{U}_j = \frac{2}{T_j w_j} \int_0^{T_j/2} \int_0^{w_j} \underline{u} \cdot \underline{n}_j ds dt, \qquad \bar{\rho}_j = \frac{2}{T_j w_j} \int_0^{T_j/2} \int_0^{w_j} \rho ds dt, \tag{1}$$

where $\underline{u}(s,t)$ and $\rho(s,t)$ are the time-dependent velocity and density, respectively, with s the coordinate across the slit, i.e. $s \in [0, w_j]$. Furthermore, $\underline{n}_j$ is the normal vector into the external flow domain, w_j is the width of the slit and $T_j = 1/f_j$ is the period of actuation, with f_j the actuation frequency. We assume the ejection part corresponds to the first half of the actuation cycle. From a dimensional analysis for a general configuration, it follows that the aerodynamic properties of the airfoil, expressed for example by the lift coefficient c_l and the drag coefficient c_d, are a function of main flow parameters, geometric parameters and actuation parameters. They are:

- main flow parameters: the angle of attack α, the Reynolds number $Re_c = \frac{\rho_\infty U_\infty c}{\mu_\infty}$, and the Mach number $M_\infty = \frac{U_\infty}{a_\infty}$,
- geometric parameters: the chordwise location of the center of the slit x_j/c, the relative slit width w_j/c, and the angle of the jet with respect to the airfoil surface θ_j,
- actuation parameters: the dimensionless actuation frequency $F^+ = \frac{f_j c}{U_\infty}$, the momentum coefficient $c_\mu = \frac{\bar{\rho}_j \bar{U}_j^2 w_j}{\rho_\infty U_\infty^2 c}$ and the relative density $\frac{\bar{\rho}_j}{\rho_\infty}$.

Since it was not feasible to do a full parameter study, some parameters have been fixed. The direction of the jet has been fixed as being perpendicular to the local surface of the airfoil, i.e. $\theta_j = 90°$. Furthermore, the relative width of the jet has been fixed at $w_j/c = 1/165$: a chord length of $c = 165$ mm together with a slit width of $w_j = 1$ mm has been used in the experiments, and therefore in the numerical simulations as well. The flow will be nearly incompressible for all experiments and numerical simulations, i.e. $M_\infty = \mathcal{O}(0.1)$ and $\bar{\rho}_j/\rho_\infty \approx 1$. The maximum Reynolds number used in the experiments and numerical simulations is 5.5×10^5, which is much lower than typical Reynolds numbers for wind turbine blades. To avoid flow features observed in low-Reynolds number flow, e.g. laminar separation bubbles, the airfoil in the experiments has turbulator strips placed close to the leading edge. In the numerical simulations, the turbulence model is used in a fully turbulent mode such that transition also occurs close to the leading edge.

3.2. Experimental Setup

A sketch of the cross section of the experimental model is shown in figure 4. It is a single piece extruded aluminum with a chord length of $c = 165$ mm and a span of $b = 90$ cm, equal to the width of test section of the wind tunnel. Based on a study by Bootsma [16], at $x_j/c = 0.06$ on both sides of the model, Streifeneder zig-zag tape is located with a thickness of 0.4 mm, width of 6 mm and a 70° zig-zag angle.

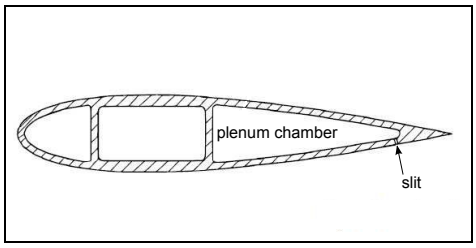

Figure 4. Cross-section of NACA0018 airfoil used in experiments.

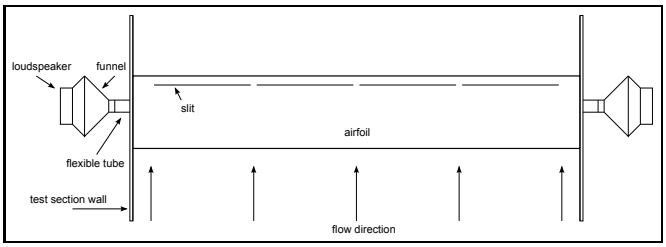

Figure 5. Sketch of experimental model (from below)

The model has three separate internal cavities, of which the aft cavity is used as a plenum chamber for synthetic jet actuation. Four rectangular slits with a width of $w_j = 1$ mm and a length of 200 mm are located on the lower side of the airfoil at $x_j/c = 0.88$, see figures 4 and 5. The spanwise distance between successive slits is 10 mm. Two externally mounted, high-quality loudspeakers (JBL 2206H/J) provide the fluctuating pressure inside the plenum, producing a synthetic jet through the slits. The loudspeakers are rated at nominally 600 W peak power.

The model is equipped with 29 pressure taps, which are round holes with a diameter of 0.5 mm, distributed over its upper and lower surface. Each pressure tap is connected to one of two pressure scanners from Esterline (9816-6496 and 9816-6498) using silicon tubes. The velocity distributions in the synthetic jets are measured by hot wire anemometry (HWA), using a Dantec hot wire probe (55P11) with a length of 1.2 mm and a diameter of 5 µm. The sampling rate is set at 25 kHz and low-pass filtering is applied at 10 kHz.

The model is located in a test section of the closed-loop Silent Wind Tunnel at the University of Twente. The test section has a width of 0.9 m, a height of 0.7 m, and a length of 2.25 m. The maximum velocity in the test section is $U_\infty = 70$ m/s and the free-stream turbulence level at the entrance of the test section is 0.4% up to $U_\infty = 50$ m/s [17].

3.3. Numerical Method

In the present study, an in-house computational method is used, which solves the Reynolds-Averaged Navier-Stokes equations for time-dependent compressble flow (URANS) in two or three dimensions. The discretization is a cell-centered finite-volume discretization on unstructured grids, which is second order accurate in time and space. The viscous fluxes employ a central scheme, whereas the convective fluxes employ Roe's flux-difference splitting scheme [18], combined with a linear reconstruction of the variables at the faces of the control volumes [19]. For the present flow simulations, a gradient limiter has not been used. The semi-discretized equations are integrated in time in an implicit manner, using dual-time stepping with Block Symmetric Gauss-Seidel iteration, accelerated by an algebraic multigrid method.

The URANS equations are closed by a linear eddy-viscosity turbulence model. In the present flow simulations, the two-equation Shear Stress Transport (SST) turbulence model [20, 21] has been used, which is solved up to the wall of the airfoil (without wall functions), in a loosely coupled manner to the URANS equations. The equations of the turbulence model are discretized also employing a second-order accurate scheme, except for the convective fluxes, for which a first-order accurate upwind scheme is employed. As recommended by Spalart & Rumsey [22], the SST turbulence model operates in a fully turbulent mode, by specifying the recommended ambient values of the turbulence variables at the inlet of the computational domain and adding a source term to the turbulence equations that prevents eddy-viscosity levels to decay between the inflow boundary and the airfoil. The resulting free-stream eddy-viscosity ratio is $\mu_t/\mu = 2 \cdot 10^{-7} Re_c$.

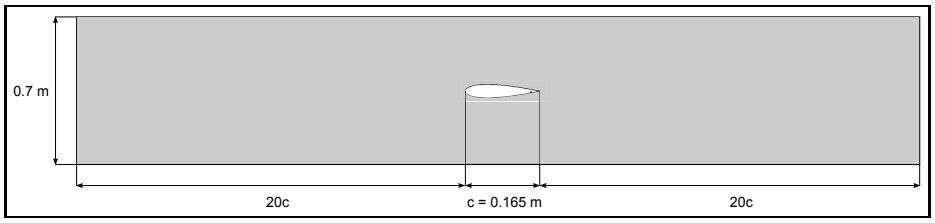

Figure 6. Sketch of computational domain, not to scale.

The computational domain used in the numerical simulations is a purely two-dimensional version of the experimental setup, see figure 6. The entrance and exit of the 'numerical test section' are located 20 chord lengths in the upstream and downstream direction, respectively. Based on the observations of Rumsey [23], the actual slit and a part of the cavity below the slit are included in the computational domain. See figure 7 for more details.

A hybrid mesh has been constructed using the open source grid generator Gmsh [24]. The original NACA0018 airfoil has been extended to zero thickness at $x/c = 1.00893$. Subsequently, the aifoil has been scaled such that the trailing edge is located at $x/c = 1$ again. To resolve the boundary layer and the synthetic jet accurately, a layer of thickness $c/4$ with quadrilaterals has been constructed along the airfoil contour and its wake line, which extends one chord length in the downstream direction. Based on a grid refinement study for baseline cases without actuation, this layer with quadrilaterals has 138 points in the normal direction with a stretching ratio of 1.05. This arrangement yields a maximum

value for the dimensionless wall distance of the first layer of cells at the wall of $y^+ \approx 1$, for $Re_c = 5.5 \times 10^5$ and $\alpha = 9°$. Along the upper side of the airfoil there are 171 points, clustered around the leading and trailing edge. The lower side of the airfoil has 304 points, including 51 points across the width of the jet. Here, the points are clustered around the leading and trailing edge of the airfoil, as well as the orifice of the jet. In the wake of the airfoil, a relatively fine mesh is constructed, with 801 points along the wake line. The bottom of the actuator cavity is discretized using 151 points, the two side walls are described by 51 points, the top of the cavity has 51 points on either side of the slit, whereas the two walls of the slit have 171 points. The rest of the domain is filled with triangular elements. The total number of elements is approximately 338000.

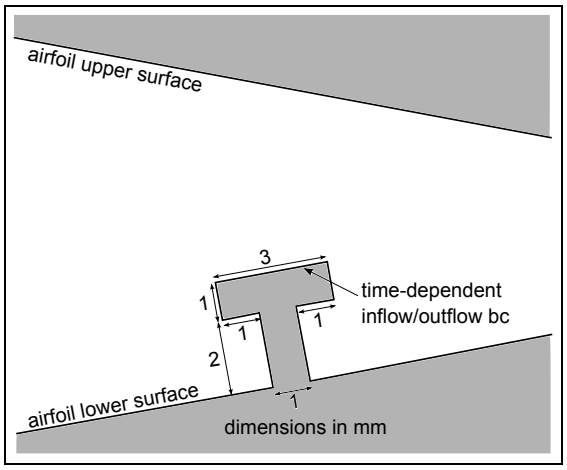

Figure 7. Close-up of computational domain near synthetic jet.

At the bottom of the actuator cavity, a time-dependent inflow/outflow boundary condition is applied, with a uniform velocity profile in space and a sinusoidal profile in time. With this technique, the jet has time and space to develop, while time-consuming boundary movement and re-meshing is avoided. The airfoil surface, as well as the rest of the internal boundaries of the synthetic jet, use adiabatic no-slip boundary conditions. At the upper and lower walls of the wind tunnel, a slip boundary condition is applied, which avoids having to resolve the boundary layers along these walls. Furthermore, a constant free-stream density and velocity is prescribed at the entrance of the domain, and a free-stream static pressure is prescribed at the exit of the domain.

4. Results

4.1. Performance of the Synthetic Jets in the Experiments

Velocity measurements of the synthetic jets show reasonable performance in terms of maximum velocity and uniformity in spanwise direction up to a frequency of approximately 120 Hz. The velocity increases (almost linearly) with the applied voltage on the loudspeakers. The highest peak velocity of 60 m/s is observed at a frequency of 15 Hz, the lowest frequency used in the experiments. The performance of the present system to generate the synthetic jets degrades for higher frequencies: the highest peak velocity at 120 Hz is 40 m/s. This means that the experimental setup can only cover very low dimensionless frequencies: for a free-stream velocity of $U_\infty = 50$ m/s, the maximum attainable value is $F^+ \approx 0.4$. For a real-scale wind turbine blade section, with a chord length at least one order of magnitude larger than that of the present wind-tunnel model, the actuation frequency becomes in the order of 10 Hz. Even for a very low free-stream velocity of $U_\infty = 16$ m/s, the maximum dimensionless frequency is still $F^+ \approx 1.24$. Since this is not in a feasible range of actuation frequencies to be used for load control, which will become clear in the following sections, we will focus on the numerical results from this point on.

4.2. Performance of the Synthetic Jets in the Numerical Simulations

The performance of the synthetic jet in terms of the momentum coefficient c_μ is a function of the applied boundary condition at the bottom of the cavity. The parameters of the boundary condition are the velocity amplitude, U_{bnd}, and the actuation frequency,

f_j. Figure 8 shows the performance for values of F^+ between 1 and 30 as a function of $(U_{bnd}w_{bnd})\,/\,(U_\infty w_j)$. The free-stream parameters are $\alpha = 0$, $Re_c = 5.50 \cdot 10^5$, $M_\infty = 0.146$, and the geometric parameters of the jet are $x_j/c = 0.88$, $w_j/c = 0.00606$. It can be seen that higher frequencies yield a higher performance. Furthermore, the relation between the velocity amplitude at the bottom of the cavity and the momentum coefficient is close to quadratic. Although not shown here, for the synthetic jet positioned at $x_j/c = 0.95$ the results are very close to the results for $x_j/c = 0.88$.

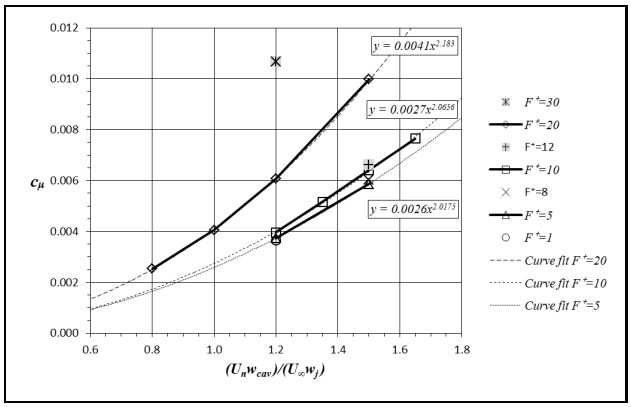

Figure 8. Performance of synthetic jet in numerical simulations, for $\alpha = 0$, $Re_c = 5.50 \cdot 10^5$, $M_\infty = 0.146$, $x_j/c = 0.88$, $w_j/c = 0.00606$.

4.3. Results for $\alpha = 0$

For an angle of attack $\alpha = 0$, a Reynolds number of $Re_c = 5.50 \cdot 10^5$ and Mach number of $M_\infty = 0.146$, we have investigated the influence on the performance of the airfoil of the dimensionless actuation frequency, F^+, the momentum coefficient, c_μ, and the jet location, x_j/c.

Figure 9(a) shows the response of the lift and drag coefficients for $F^+ = 20$, $c_\mu = 0.0061$, $x_j/c = 0.88$, using 80 time steps per actuation cycle. Figure 9(b) shows the response during one cycle in the periodic state ($U_\infty t/c > 12$). For this case, the average increase of the lift coefficient in the periodic state is $\Delta c_l = 0.092$, which corresponds to an effective change of the angle of attack of approximately 1 degree. The required actuator power is 175 W per meter span. It is evident that there is a large amplitude of the lift coefficient with respect to its average increase. The difference between the maximum and minimum value per cycle, i.e. $c_{l,\max} - c_{l,\min}$, is 0.32. However, since the actuation frequency is very high, it is virtually 'invisible' to the structure: the natural frequencies of wind turbine blades are much lower. When the pressure distribution on the airfoil is averaged during a cycle, the resulting distribution is quite smooth, as can be seen in figure 14 (solid line corresponds to the present case). The calculated c_d without actuation is $c_d = 0.014242$, whereas the average c_d with actuation for this case is $c_d = 0.01546$, i.e. an increase of approximately 12 drag counts. The difference between the maximum and minimum value per cycle is $c_{d,\max} - c_{d,\min} = 0.055$.

The nondimensional time needed to reach the periodic state is approximately $12U_\infty t/c$. Approximately 50% of the total increase in lift is obtained within $2U_\infty t/c$, which is important since it indicates the potential for rapid load control. Note that the response in lift starts off with a small decrease before it starts to rise. This is due to a low-pressure region that builds up downstream of the jet. As soon as this low-pressure region has reached the trailing edge, the pressure distribution on the upper side of the airfoil reacts and the lift starts to increase.

Figure 10 shows instantaneous streamlines and iso-contours of the dimensionless vorticity, $\omega_z c/U_\infty$, in the region near the trailing edge at different phases during the

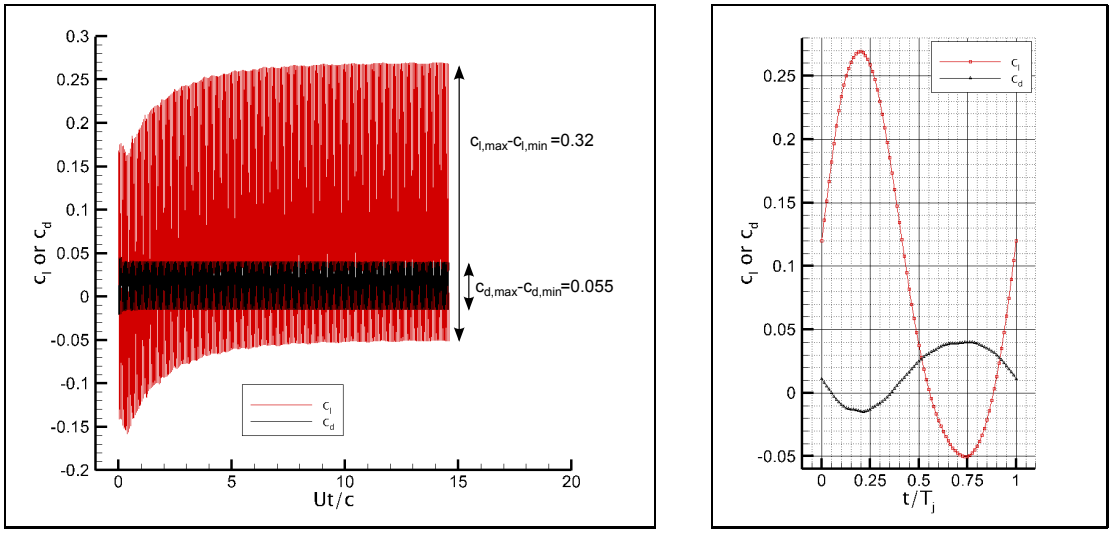

a: all cycles b: one cycle in periodic state

Figure 9. Response of c_l and c_d to actuation as a function of $U_\infty t/c$ (a) and during one cycle in periodic state (b), for $\alpha = 0$, $Re_c = 5.50 \cdot 10^5$, $M_\infty = 0.146$, $x_j/c = 0.88$, $w_j/c = 0.00606$, $F^+ = 20$ and $c_\mu = 0.0061$.

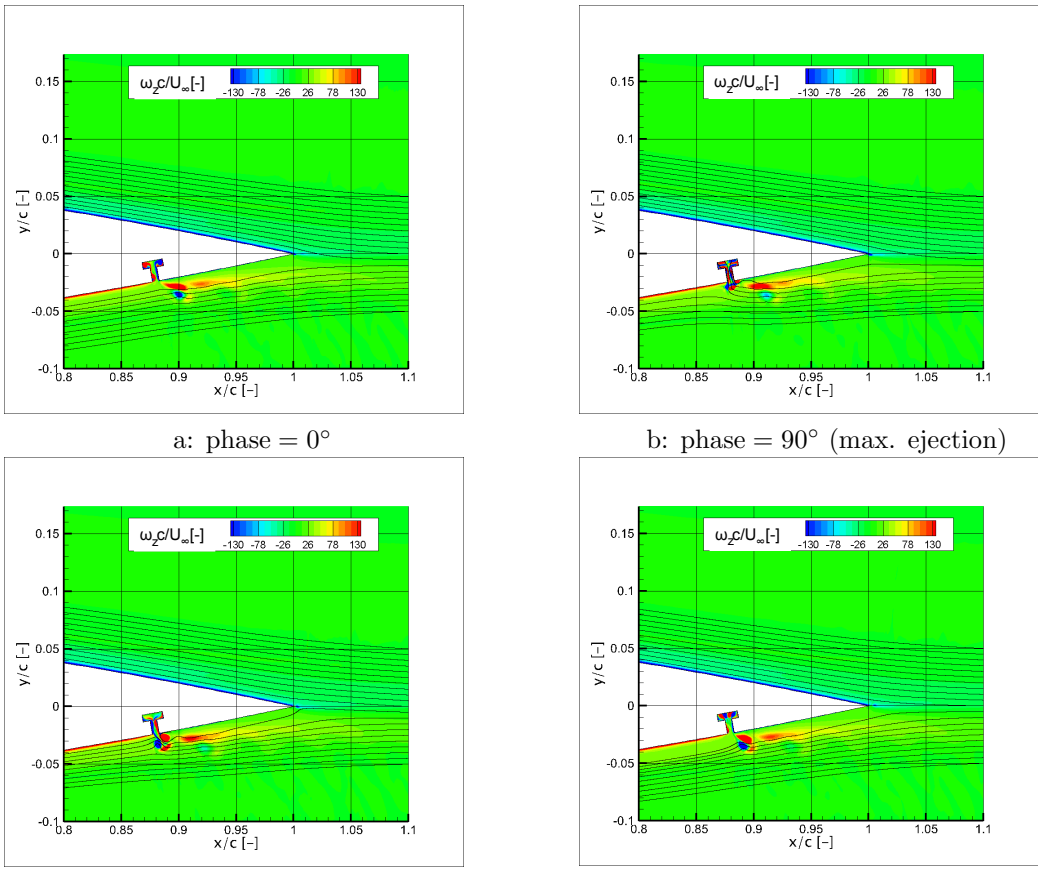

a: phase = 0° b: phase = 90° (max. ejection)

c: phase = 180° d: phase = 270° (max. ingestion)

Figure 10. Streamlines and iso-contours of nondimensional vorticity in trailing edge region at different phases during actuation cycle, for $\alpha = 0$, $Re_c = 5.50 \cdot 10^5$, $M_\infty = 0.146$, $x_j/c = 0.88$, $w_j/c = 0.00606$, $F^+ = 20$ and $c_\mu = 0.0061$.

actuation cycle. Vortices can be seen to emerge from the slit. Those with a negative sign are rapidly dissipated, whereas a train of vortices with a positive sign (counter-clockwise) remains visible for a certain distance. This train of vortices becomes an obstruction for the main flow along the lower side of the airfoil. This effectively changes the Kutta condition at the trailing edge, i.e. on the average the circulation of the airfoil increases.

The range of c_μ that has been currently investigated corresponds to $\bar{U}_j/U_\infty \in [0.65, 1.31]$. Since $\bar{U}_j$ is an average jet velocity over the jet width and ejection part of the actuation cycle, the relative peak velocity at maximum ejection is much higher. Figure 11 shows the velocity profile across the exit of the slit at different phases during the actuation cycle, for $x_j/c = 0.88$, $F^+ = 20$ and $c_\mu = 0.0061$. This momentum coefficient corresponds to $\bar{U}_j/U_\infty = 1.0$, and has been obtained using $(U_{bnd} w_{bnd}) \,/\, (U_\infty w_j) = 1.2$. Note that the peak velocities are in the order of $2U_\infty$ to $2.5U_\infty$ for this case. It is expected that still higher values of c_μ are not realistic.

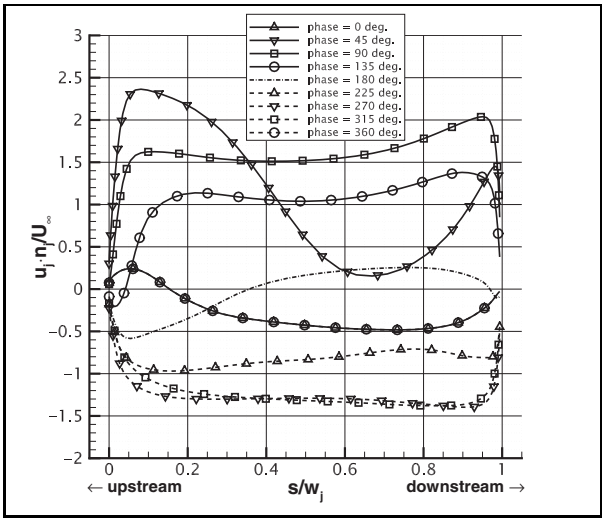

Figure 11. Profiles of normal velocity across slit at different phases during actuation cycle for $\alpha = 0$, $Re_c = 5.50 \cdot 10^5$, $M_\infty = 0.146$, $x_j/c = 0.88$, $w_j/c = 0.00606$, $F^+ = 20$ and $c_\mu = 0.0061$ (corresponds to $\bar{U}_j/U_\infty = 1.0$).

Figure 12 shows the increase in time-averaged lift coefficient, Δc_l, as a function of the momentum coefficient, c_μ, for different dimensionless actuation frequencies, F^+, and the jet located at $x_j/c = 0.88$. Δc_l has been determined over a number of actuation cycles when the results have become periodic. The result for $F^+ = 1$ has been calculated using 400 time steps per cycle, whereas all other results have been calculated with 80 time steps per cycle. In general, for a fixed F^+, the time-averaged lift increases with increasing c_μ. Note that there is no increase in the time-averaged lift coefficient for $F^+ = 1$, but a small decrease. Of all computed cases, the largest increase of the time-averaged lift for a jet location of $x_j/c = 0.88$ is obtained for $F^+ = 10$ and equals $\Delta c_l = 0.192$. This corresponds to an effective change of the angle of attack of approximately 2 degrees. However, for higher values of c_μ, the lift increment might further increase.

Locating the jet closer to the trailing edge of the airfoil also increases the lift increment, see figure 13. The largest increase of the computed cases for $x_j/c = 0.95$ is $\Delta c_l = 0.224$, which corresponds to a change of the angle of attack of approximately 2.5 degrees.

Figure 14 shows that the entire time-averaged pressure distribution is positively affected by shifting the synthetic jet towards the trailing edge. This shift has the additional benefit of reducing the response time: the nondimensional time needed to obtain 50% of the final increase in lift for $x_j/c = 0.95$ is approximately $U_\infty t/c$, a reduction of 50% with respect

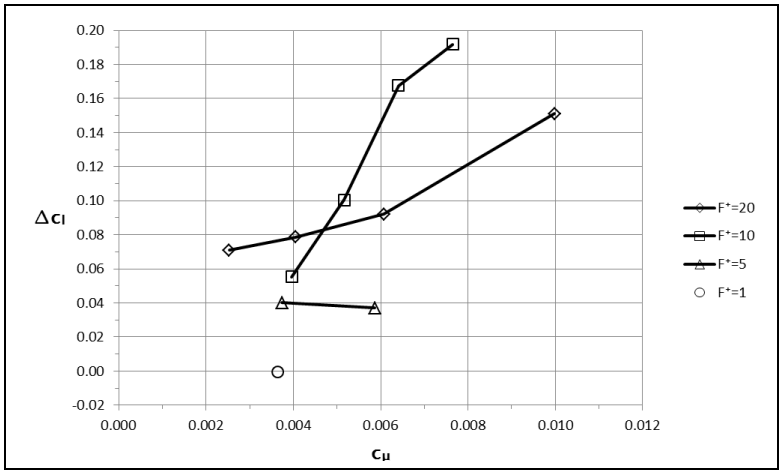

Figure 12. Increase of time-averaged lift coefficient as a function of c_μ for different F^+, and $\alpha = 0$, $Re_c = 5.50 \cdot 10^5$, $M_\infty = 0.146$, $x_j/c = 0.88$, $w_j/c = 0.00606$.

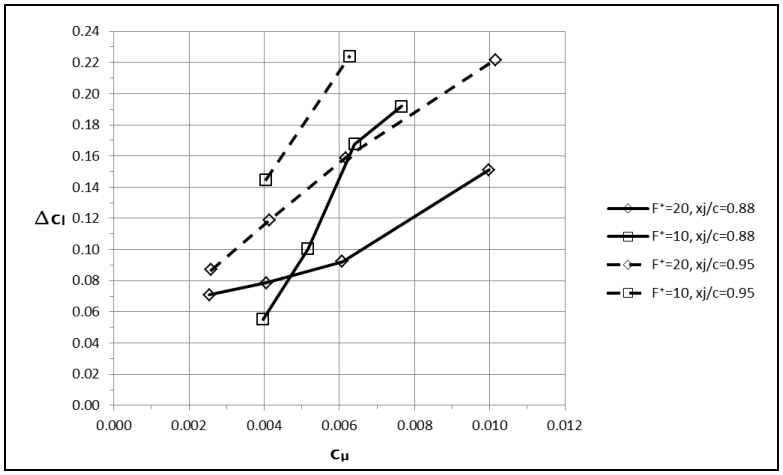

Figure 13. Increase of time-averaged lift coefficient as a function of c_μ for different F^+ and x_j/c, and $\alpha = 0$, $Re_c = 5.50 \cdot 10^5$, $M_\infty = 0.146$, $w_j/c = 0.00606$.

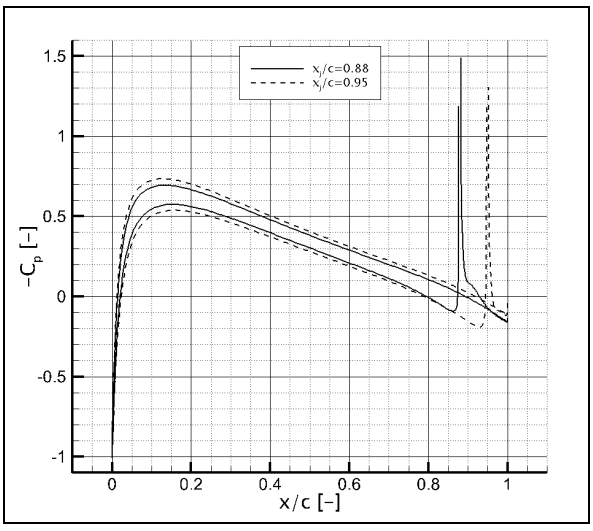

Figure 14. Time-averaged pressure distribution for different x_j/c, $\alpha = 0$, $Re_c = 5.50 \cdot 10^5$, $M_\infty = 0.146$, $w_j/c = 0.00606$, $F^+ = 20$ and $c_\mu \approx 0.006$

to the case for $x_j/c = 0.88$.

The increase in time-averaged lift comes with a drag penalty, as shown in figure 15. It is interesting to note that the drag penalty decreases when the jet location is closer to the trailing edge.

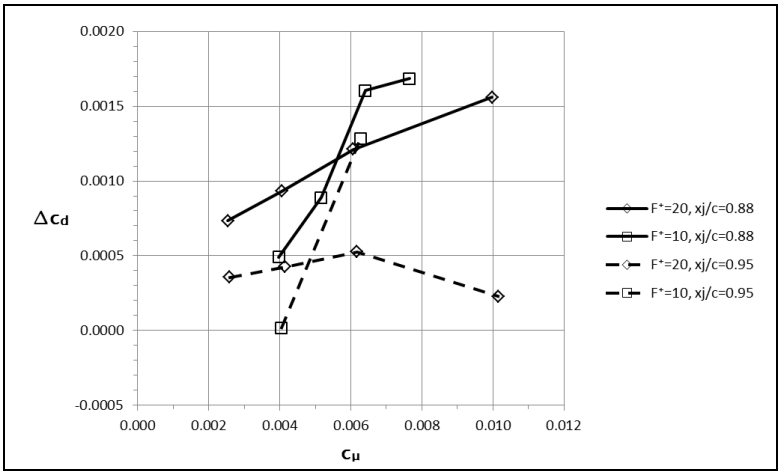

Figure 15. Increase of time-averaged drag coefficient as a function of c_μ for different F^+ and x_j/c, and $\alpha = 0$, $Re_c = 5.50 \cdot 10^5$, $M_\infty = 0.146$, $w_j/c = 0.00606$.

4.4. Results for $\alpha = 9$ degrees

For an angle of attack of $\alpha = 9$ degrees, the lift over drag ratio is close to its maximum value. This corresponds to the normal operating condition of a wind turbine blade. At this angle of attack, the flow on the suction side of the airfoil has separated near the trailing edge. For this situation we have also performed numerical simulations of synthetic jet actuation, and the results can be summarized briefly as follows:

- In general, the performance in terms of an increase of the time-averaged lift coefficient is lower for the higher angle of attack and the same values of F^+ and c_μ. This is due to a smaller thickness of the boundary layer along the airfoil just upstream of the synthetic jet at the higher angle of attack, which is associated with a higher momentum in the cross-flow close to the wall. This reduces the ability of the synthetic jet to form an obstruction to the main flow.
- For reasonable values of the momentum coefficient, c_μ, the dimensionless actuation frequency needs to be at least $F^+ = 20$ to obtain any positive change of the lift coefficient.
- The maximum obtained increase of the time-averaged lift coefficient in this study for $\alpha = 9°$ equals $\Delta c_l = 0.317$ ($\Delta\alpha \approx 2.9°$), which is obtained for $F^+ = 20$, $c_\mu \approx 0.01$ and $x_j/c = 0.985$, i.e. a location of the slit very close to the trailing edge.

5. Concluding Remarks

Computational results show that the present configuration of synthetic jet actuation could be used for load control. For high actuation frequencies, $F^+ = \mathcal{O}(10)$, a train of separate vortices emerge from the slit, which can effectively become an obstacle to the flow along the airfoil. A low-pressure region can be formed between the slit and the trailing edge, which attracts the flow from the upper side of the airfoil. This deflects the flow at the trailing edge downwards and therewith increases the circulation and therefore the lift. Approximately 50% of the final increase in lift can be obtained within $U_\infty t/c$. In general, the time-averaged lift increases with increasing momentum coefficient, c_μ, and locations of

the slit, x_j/c, closer to the trailing edge. The latter option also reduces the drag penalty associated with synthetic jet actuation.

For higher angles of attack, the performance of synthetic jet actuation reduces. Still, for reasonable values of the momentum coefficient, c_μ, the performance can be sustained for $F^+ = 20$ and a location of the slit very close to the trailing edge: $x_j/c = 0.985$.

Further research is needed to optimize the configuration of the synthetic jet. Furthermore, the effect of synthetic jet actuation at negative angles of attack should also be investigated.

The experimental setup showed severe degradation of performance of the synthetic jets for high actuation frequencies, i.e. the frequencies that we are interested in. Probably a different setup with an array of built-in actuators is needed in order to obtain the necessary velocity magnitude with an adequate spanwise uniformity. Currently, the results for low actuation frequencies are used for validation of the numerical method.

References

[1] Barlas T K and Van Kuik G A M 2007 *Journal of Physics: Conference Series* **75** 012080
[2] Van Kuik G A M 2011 Final report, showing the potential of smart rotor blades and rotor control Upwind Work Package 1B3, deliverable 12
[3] Johnson S J, van Dam C P and Berg D E 2008 Active load control techniques for wind turbines Sandia Report SAND2008-4809
[4] Johnson S J, Baker J P, van Dam C P and Berg D 2010 *Wind Energy* **13** 239 – 253
[5] Glezer A and Amitay M 2002 *Annual Review of Fluid Mechanics* **34** 503 – 529
[6] Boeije C S, de Vries H, Cleine I, van Emden E, Zwart G G M, Stobbe H, Hirschberg A and Hoeijmakers H W M 2009 Fluidic load control for wind turbine blades AIAA Paper 2009-684
[7] Johansen J, Sørensen N N, Zahle F, Kang S, Nikolaou I, Politis E S, Chaviaropoulos P K and Ekaterinaris J 2004 Know-blade task-2 report; aerodynamic accessories Risø Report 1482(EN)
[8] Maldonado V, Farnsworth J, Gressick W and Amitay M 2008 Active enhancement of wind turbine blades performance AIAA Paper 2008-1311
[9] Lopez O D, Moser R D, Brzozowski D P and Glezer A 2009 Aerodynamic performance of airfoils with tangential synthetic jet actuators close to the trailing edge AIAA Paper 2009-3674
[10] DeSalvo M E, Amitay M and Glezer A 2002 Modification of the aerodynamic performance of airfoil at low angle of attack: Trailing edge trapped vortices AIAA paper 2002-3165
[11] DeSalvo M E and Glezer A 2004 Aerodynamic performance modification at low angles of attack by trailing edge vortices AIAA Paper 2004-2118
[12] DeSalvo M E and Glezer A 2005 Airfoil aerodynamic performance modification using hybrid surface actuators AIAA Paper 2005-0874
[13] Shea P R and Smith D R 2009 Aerodynamic control of a rectangular wing using gurney flaps and synthetic jets AIAA Paper 2009-886
[14] Seifert A, Bachar T, Koss D, Shepshelovich M and Wygnanski I 1993 *AIAA Journal* **31** 2052 – 2060
[15] Amitay M and Glezer A 2002 *AIAA Journal* **40** 209 – 216
[16] Bootsma K 2011 De invloed van turbulatoren op de grenslaag van een profiel van een windturbine blad (the influence of turbulators on the boundary layer of a wind turbine blade section) BSc thesis University of Twente
[17] Zwart G G M 2008 Turbulence measurements 130 kw wind tunnel Technical report, Engineering Fluid Dynamics, University of Twente
[18] Roe P L 1981 *Journal of Computational Physics* **43** 357 – 372
[19] van Leer B 1979 *Journal of Computational Physics* **32** 101 – 136
[20] Menter F R 1992 Improved two-equation k-ω turbulence models for aerodynamic flows NASA TM 103975
[21] Menter F R, Kuntz M and Langtry R 2003 *Turbulence, Heat and Mass Transfer 4* ed Hanjalic K, Nagano Y and Tummers M (Begell House, Inc.) pp 625 – 632
[22] Spalart P R and Rumsey C L 2007 *AIAA Journal* **45** 2544 – 2553
[23] Rumsey C L 2008 Successes and challenges for flow control simulations AIAA Paper 2008-4311
[24] Geuzaine C and Remacle J F 2009 *International Journal for Numerical Methods in Engineering* **79** 1309 – 1331